Research Article | Vol. 27, No. 6 | 18 Mar 2019 | OPTICS EXPRESS 8800
Optics EXPRESS

Liquid crystal tunable terahertz lens with spin-selected focusing property

ZHIXIONG SHEN,[1,2] SHENGHANG ZHOU,[1] SHIJUN GE,[1,2,3] WEI DUAN,[1] LINGLING MA,[1] YANQING LU,[1] AND WEI HU[1,2,*]

[1]National Laboratory of Solid State Microstructures, Key Laboratory of Intelligent Optical Sensing and Manipulation, Collaborative Innovation Center of Advanced Microstructures, College of Engineering and Applied Sciences, Nanjing University, Nanjing 210093, China
[2]Institute for Smart Liquid Crystals, JITRI, Changshu 215500, China
[3]geshijun@nju.edu.cn
[*]huwei@nju.edu.cn

Abstract: We propose and demonstrate an active spin-selected lens with liquid crystal (LC) in the terahertz (THz) range. The lens is a superposition of two geometric phase lenses with separate centers and conjugated phase profiles. Its digitalized multidirectional LC orientations are realized via a dynamic micro-lithography-based photo-patterning technique and sandwiched by two graphene-electrode-covered silica substrates. The specific lens can separate the focusing spots of incident light with opposite circular polarizations. Its focusing performance from 0.8 to 1.2 THz is characterized using a scanning near-field THz microscope system. The polarization conversion efficiency varies from 32.1% to 70.2% in this band. The spin-selected focusing functions match well with numerical simulations. Such lens exhibits the merit of dynamic functions, low insertion loss and broadband applicability. It may inspire various practical THz apparatuses.

1. Introduction

Terahertz (THz) lies between the visible and microwave and is the last electromagnetic spectrum to be explored [1,2]. Due to the lack of natural materials to modulate THz wave, fundamental THz modulators are imperative. Among them, THz lens [3–5] is a key requirement for its wide applications in high resolution THz imaging and wireless communication [6,7]. Commonly, they are accomplished via controlling the phase accumulation along propagation of polished crystals or polymers. Such devices are heavy and bulky and could not satisfactorily match the miniaturization and integration tendency of THz elements. Metasurface lens, composed of subwavelength metallic or dielectric resonator arrays, can manipulate the THz wavefront in a compact manner [8,9]. By this means, polarization-dependent focusing, super-resolution focusing and micro-lens arrays are reported [10–12]. However, they still suffer from low polarization conversion efficiency (PCE) and static functionalities. To realize active and efficient design is highly demanded in THz field.

Liquid crystal (LC) lens is well documented in the visible range due to its splendid electro-tunability [13–16]. Its THz counterpart has been expected for a long time. Until recently, the electric driving and alignment for extremely thick cells have been settled [17,18]. Tunable phase retarder [19], active filters [20,21] and vortex beam generators [22,23] are presented subsequently. Compared to metasurface, LC is non-resonant and the conversion efficiency of the generated wave is determined only by the phase retardation. Therefore, it allows a much higher PCE. Additionally, the LC orientation can be realigned by external fields, *e.g.* electric or magnetic fields [24,25], making the device tunable or switchable. It supplies a promising strategy for realizing tunable and efficient LC THz lens.

In this paper, a spin-selected THz lens is proposed and demonstrated by a large birefringent LC with spatially variant orientations. With this sample, THz wave of opposite

#358577 https://doi.org/10.1364/OE.27.008800
Journal © 2019 Received 24 Jan 2019; revised 27 Feb 2019; accepted 3 Mar 2019; published 11 Mar 2019

Optics EXPRESS

spin states can be focused to two separate spots. The focusing performance in a broad band is numerically simulated and experimentally characterized, which matches well with each other. Driven by graphene transparent electrodes [18,26], THz wave are efficiently tuned and switched. This work may facilitate applications in THz communication and imaging.

2. Design and principle

The decomposed configuration of the device is illustrated in Fig. 1(a). Both substrates are 800-μm-thick fused silica. After ultrasonically cleaned, substrates are transferred with graphene (Six Carbon Technology, Shenzhen, China). Then the alignment layer sulfonic azo dye (SD1, Dainippon Ink and Chemicals Inc., Chiba, Japan) [27,28] is spincoated onto the graphene. Afterwards, the two substrates are assembled and separated by 250-μm-thick Mylar spacer to form a cell. A digital micro-mirror device based dynamic micro-lithography [29] is employed to control the spatial distribution of LC directors in order to realize the desired phase diagram exhibited in Fig. 1(c). After an LC NJU-LDn-4 [30] with an average birefringence over 0.3 from 0.5 to 2.0 THz is infiltrated, the obtained LC orientation presented in Fig. 1(b) agrees well with the design.

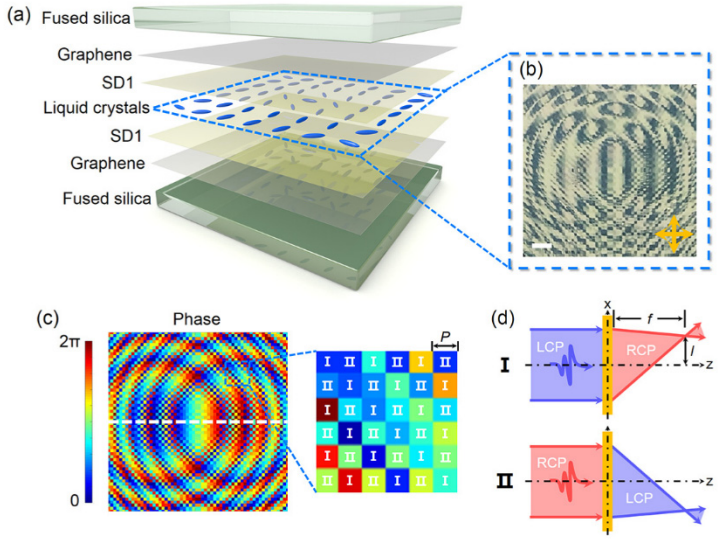

Fig. 1. (a) The schematic illustration of the spin-selected lens. (b) The photo of the sample under crossed polarizers (indicated by two yellow arrows). Scale bar: 1 mm. (c) The designed phase diagram. Inset shows a magnified 6 × 6 pixel array, which is divided into lattice I and II. The lattice periodicity p is 152 μm. (d) The focusing functions of lattice I and II.

The lens function originates from the geometric phase determined by the LC orientation. For a homogeneously aligned LC domain with orientation angle α, its Jones matrix is:

$$\begin{aligned}\mathbf{J} &= \mathbf{R}(-\alpha)\cdot\begin{pmatrix}\exp(-i\zeta) & 0\\ 0 & \exp(i\zeta)\end{pmatrix}\cdot\mathbf{R}(\alpha)\\ &= -i\sin\zeta\cdot\begin{pmatrix}\cos 2\alpha & \sin 2\alpha\\ \sin 2\alpha & -\cos 2\alpha\end{pmatrix}+\cos\zeta\cdot\mathbf{I},\end{aligned} \tag{1}$$

where $\mathbf{R}$ is the rotation matrix, $\mathbf{I}$ is the identity matrix, $\zeta = \pi\delta nd/\lambda$ is half of the phase retardation, δn, d and λ are LC birefringence, cell gap and incident wavelength, respectively. The normalized Jones vector is $\chi^{(+)} = (1, +\mathrm{i})^{\mathrm{T}}/\sqrt{2}$ for left circular polarization (LCP) and $\chi^{(-)}$

Optics EXPRESS

= $(1, -i)^T/\sqrt{2}$ for right circular polarization (RCP). When a circular polarized wave incidents, the output wave is described as:

$$\mathbf{E}_{out} = \mathbf{J} \cdot \chi^{(\pm)} = -i \sin\zeta \cdot \exp(\pm i2\alpha) \cdot \chi^{(\mp)} + \cos\zeta \cdot \chi^{(\pm)}. \quad (2)$$

For LCP incident wave, the output wave is devided into two parts. One is the residual LCP component with no extra phase modulation. The other is the transformed RCP component with a phase factor $\exp(i2\alpha)$. Vice verse.

The phase function for a traditional convex lens is expressed as:

$$\varphi(x, y) = -2\pi(\sqrt{f^2 + x^2 + y^2} - f)/\lambda, \quad (3)$$

where (x, y) is the coordinate in the plane normal to the propagation and f is the focal length. For a geometric phase lens, the phase profile is circular polarization dependent. For RCP wave, it is converted to LCP wave and focused at $(0, 0, f)$. While for LCP, it is converted to RCP and diverged. The polarization conversion efficiency is determined by the phase retardation. It could reach 100% when the device satisfies halfwave condition.

Our design is to combine two geometric phase lenses in a checkerboard pattern as shown in Fig. 1(c). The phase profile in lattice I is:

$$\varphi_{\mathrm{I}}(x, y) = +2\pi(\sqrt{f^2 + (x + l)^2 + y^2} - f)/\lambda. \quad (4)$$

The phase profile in lattice II is:

$$\varphi_{\mathrm{II}}(x, y) = -2\pi(\sqrt{f^2 + (x - l)^2 + y^2} - f)/\lambda, \quad (5)$$

where l is the deviation of the focal spot to z-axis (Fig. 1(d)). Here, φ_{I} and φ_{II} exhibit conjugated phases and separate focal spots. The color bar in Fig. 1(c) indicates the phase varying from 0 to 2π. In our work, the specific phase is demonstrated by LCs, which introduce geometric phase via controlling local LC orientations. The geometric phase is twice the LC orientation angle α. According to Fig. 1(c), the LC orientation is realized through a multi-step partly-overlapping exposure process. For such a combined geometric phase lens, the LCP incident wave is focused at $(-l, f)$ by lattice I while diverged by lattice II. It needs to be noticed that the diverging part is negligible compared to the focused one. On the contrary, the RCP incident wave will be focused at (l, f). Therefore, a spin-selected focusing function is realized.

3. Results and discussions

To verify the design, numerical simulations of the lens is carried out using a commercial simulation software, Lumerical FDTD Solutions. The simulation is carried out based on the LC orientation in consistent with the phase diagram shown in Fig. 1(c). To simplify the simulation, a model is established in the white dashed line along x-axis. Each domain is set as 150 μm × 200 μm × 250 μm. The 250-μm-thick LC is set as a diagonal dielectric material with n_o = 1.50 + i0.006 (diagonal elements xx and yy) and n_e = 1.81 + i0.001 (diagonal element zz). The LC director distributions are set by an LC orientation module. A plane wave with a spectrum range from 0.8 to 1.2 THz incidents along z-axis. The simulated THz field in the xz-plane with incident linear polarization (LP), LCP and RCP waves are shown in Figs. 2(a)-2(c), respectively. For LP, two focal spots are symmetrically separated to two sides of z-axis, with f increasing from 12.3 to 17.8 mm when the frequency changes from 0.8 to 1.2 THz (Fig. 2(a)). Figures 2(b) and 2(c) vividly show the spin-selected focusing property.

Optics EXPRESS

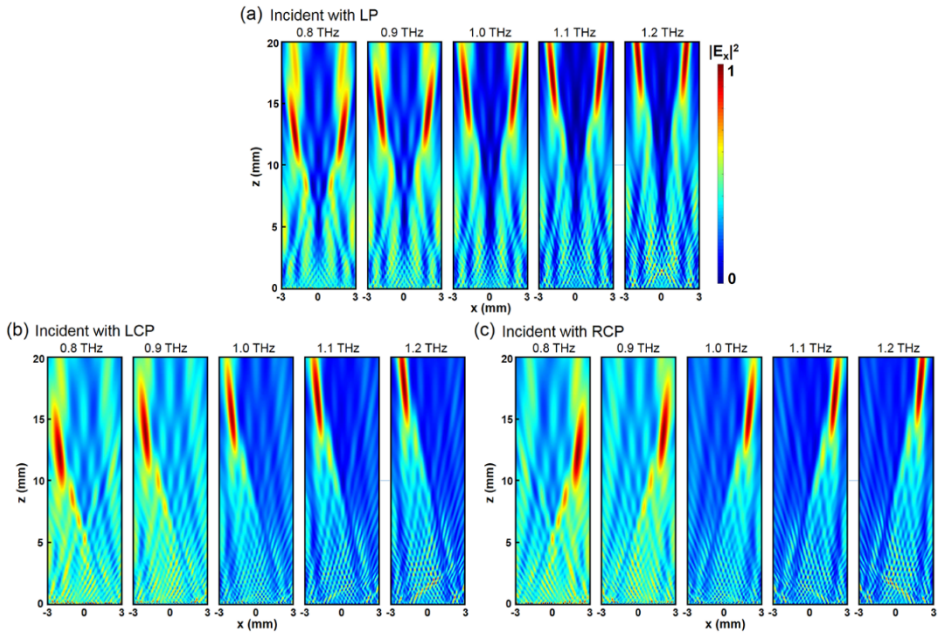

Fig. 2. The simulated normalized THz field in the *xz*-plane from 0.8 to 1.2 THz when the incident wave is (a) LP, (b) LCP and (c) RCP, respectively.

A scanning near-field THz microscope (SNTM) system is utilized to characterize the focusing performance of the lens. The system is based on photoconductive THz generation and microprobe THz detection. Briefly, a pair of metallic electrodes are deposited on a semiconductor to form a THz emitter. When a femtosecond pulse reaches it, electrons oscillate and radiate THz. The principle for detection is an inverse process of emission. The photo-generated carriers excited by the probe beam directionally move and generate a varying current under the THz wave irridation. Via detecting the current, the THz signal can be restored. Therefore, both design and materials of probe and pump elements of this system are different from normal ones. The experimental setup is illustrated in Fig. 3(a). An ultrafast laser pulse (90 fs, 780 nm, 90 MHz) is divided into two parts, the pump (10 mW) and probe (3 mW) beams for the generation and detection of the THz wave, respectively. A collimated LP THz wave ranging from 0.2 to 1.5 THz transmits through a quarter-wave plate (QWP) to generate LCP and RCP waves. The scanning tip is utilized to scan the E_x field in the *xy*-plane. The sample moves along *z*-axis to capture the THz field in the *xz*-plane.

Optics EXPRESS

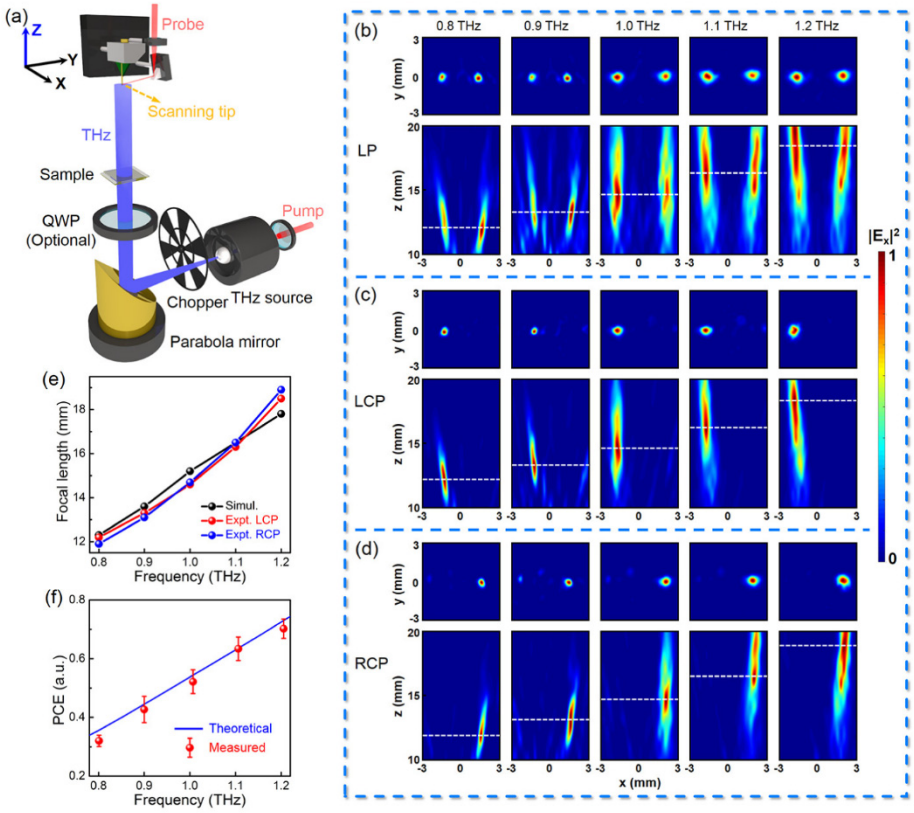

Fig. 3. (a) The experimental setup of the SNTM system. (b-d) The measured THz fields in the focal planes and *xz*-plane from 0.8 to 1.2 THz when the incident wave is (b) LP, (c) LCP and (d) RCP. (e) The dependency of focal length on frequency for LCP and RCP, respectively. (f) The dependency of PCE on frequency.

The normalized THz field in the *xy*- and *xz*-plane from 0.8 to 1.2 THz for LP, LCP and RCP incident waves are illustrated in Figs. 3(b)-3(d). When LCP wave transmits through the sample, the output wave is focused at left side of *z*-axis. While RCP wave is focused at right side of *z*-axis. The experimental data match well with the simulation results, with only a small deviation in the focal length (Fig. 3(e)). The theoretical and measured PCE from 0.8 to 1.2 THz is presented in Fig. 3(f). The theoretical one is calculated by $\sin^2(\zeta)$ from Eq. (2). To measure the PCE, a 250-μm-thick homogeneously aligned LC cell and a pair of QWPs are introduced. The front QWP is placed before the cell to generate LCP incident wave. The rear one is set behind the cell with axis orthogonal and parallel to that of the front one to select LCP (E_{LCP}) and RCP (E_{RCP}) components, respectively. PCE is calculated by $|E_{RCP}|^2/(|E_{RCP}|^2 + |E_{LCP}|^2)$. As shown in Fig. 3(f), the measured PCE increases from 32.1% to 70.2% in the range from 0.8 to 1.2 THz, which agrees with the theoretical result. This shows significant superiority to the transmission-type metasurface. It needs to be mentioned that a femtosecond laser is utilized as the pump in our system, the generated THz beam is a broadband pulse wave. Because LC elements are wavelength dependent, the halfwave condition is only satisfied for a certain frequency here. In our experiment, the SNTM is only adopted for measurements. As it is a time domain spectrometer, the obtained phase modulation at different frequencies can be extracted via Fourier transformation. Actually, single frequency or narrow band THz modulation has a lot of applications as well. Our LC THz lens is tunable and could be optimized for different frequencies via electrically tuning. Nowadays, many achromatic devices are presented in visible and near-IR range to meet the broadband

Optics EXPRESS

applications [31–33]. The design can be adopted to the fabrication of THz counterparts as well.

The lens can be dynamically switched via applying voltage to graphene electrodes. When the 1 kHz square-wave bias is 80 V (the saturated bias), the LC directors are reoriented along *z*-axis, as shown in Fig. 4(a). At this state, the lens function vanishes, thus the transmitted THz wave remains unmodulated. Measured THz fields in the *xy*-plane at 1.0 THz for incident LP, LCP and RCP are presented in Fig. 4(b). Gaussian-shape spots are observed regardless of the incident polarization. The normalized intensities at $y = 0$ in the *xy*-plane at bias OFF and saturated states with LP, LCP and RCP incident waves are compared in Fig. 4(c), vividly exhibiting the switchability of the proposed lens. Since the response time of LC is proportional to the square of the cell gap, here the responses is calculated to be in second scale. As sufficient thickness of LC is demanded to reach the halfwave condition, the slow response issue is unavoidable. Fortunately, as the switching function here is realized via circular polarization conversion, fast switching can be achieved by introducing fast responsive EO waveplates. This proof-of-concept demonstration still satisfies various applications where no fast and frequent switching is required. In addition, the response can be improved via optimizing the device design (stacking cell strategy as shown in Ref. 18) and judiciously selecting LCs.

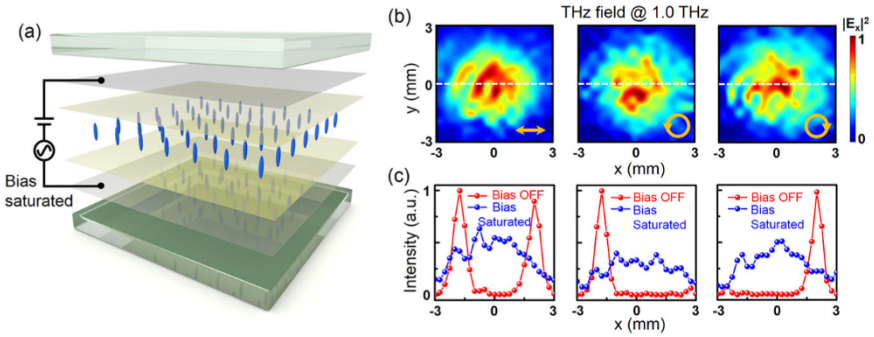

Fig. 4. (a) The schematic illustration of the device at bias saturated state. (b) The measured THz field ($z = 15$ mm, 1.0 THz) at bias saturated state when the incident wave is LP, LCP and RCP, respectively. (c) The corresponding normalized intensity at $y = 0$ in the *xy*-plane (white dashed lines in (b)) at bias OFF and saturated states with incident LP, LCP and RCP.

Such active spin-selected lens could be used as THz polarization filters or analyzers [34] and may find practical applications in polarization-based THz imaging and wireless communication [35,36]. Since many biomolecules possess THz fingerprints and are sensitive to incident polarization, the lens could be further applied to biomedical detections [37,38].

4. Conclusion

In summary, a spin-selected THz lens is proposed. The device is composed of photo-patterned LCs sandwiched by two few-layer graphene electrodes. Through elaborately designing the geometric phase profile, the lens performs the spin-dependent focusing from 0.8 to 1.2 THz with PCE varying from 32.1% to 70.2%. When a bias is applied or not, the lens function can be switched OFF/ON. This work provides a promising method for fabricating active and efficient THz apparatuses, which may be widely applicable in THz communication, imaging and biosensing.

Funding

The National Key Research and Development Program of China (2017YFA0303700), the National Natural Science Foundation of China (NSFC) (Nos. 61575093, 61490714, and 61435008), the Distinguished Young Scholars Fund of Jiangsu Province (BK20180004), the

Optics EXPRESS

Fundamental Research Funds for the Central Universities and Jiangsu Donghai Silicon Industry Science and Technology Innovation Center.

Acknowledgments

W. H. gratefully acknowledges the support of the Tang Scholar program.

References

1. X. C. Zhang and J. Xu, *Introduction to THz wave photonics* (Springer, 2010).
2. B. Ferguson and X. C. Zhang, "Materials for terahertz science and technology," Nat. Mater. **1**(1), 26–33 (2002).
3. B. Scherger, C. Jördens, and M. Koch, "Variable-focus terahertz lens," Opt. Express **19**(5), 4528–4535 (2011).
4. J. Neu, B. Krolla, O. Paul, B. Reinhard, R. Beigang, and M. Rahm, "Metamaterial-based gradient index lens with strong focusing in the THz frequency range," Opt. Express **18**(26), 27748–27757 (2010).
5. X. Y. Jiang, J. S. Ye, J. W. He, X. K. Wang, D. Hu, S. F. Feng, Q. Kan, and Y. Zhang, "An ultrathin terahertz lens with axial long focal depth based on metasurfaces," Opt. Express **21**(24), 30030–30038 (2013).
6. C. M. Watts, D. Shrekenhamer, J. Montoya, G. Lipworth, J. Hunt, T. Sleasman, S. Krishna, D. R. Smith, and W. J. Padilla, "Terahertz compressive imaging with metamaterial spatial light modulators," Nat. Photonics **8**(8), 605–609 (2014).
7. S. Koenig, D. Lopez-Diaz, J. Antes, F. Boes, R. Henneberger, A. Leuther, A. Tessmann, R. Schmogrow, D. Hillerkuss, R. Palmer, T. Zwick, C. Koos, W. Freude, O. Ambacher, J. Leuthold, and I. Kallfass, "Wireless sub-THz communication system with high data rate," Nat. Photonics **7**(12), 977–981 (2013).
8. N. Yu and F. Capasso, "Flat optics with designer metasurfaces," Nat. Mater. **13**(2), 139–150 (2014).
9. M. Khorasaninejad and F. Capasso, "Metalenses: Versatile multifunctional photonic components," Science **358**(6367), 6367 (2017).
10. S. Wang, X. Wang, Q. Kan, J. Ye, S. Feng, W. Sun, P. Han, S. Qu, and Y. Zhang, "Spin-selected focusing and imaging based on metasurface lens," Opt. Express **23**(20), 26434–26441 (2015).
11. X. Zang, C. Mao, X. Guo, G. You, H. Yang, L. Chen, Y. Zhu, and S. Zhuang, "Polarization-controlled terahertz super-focusing," Appl. Phys. Lett. **113**(7), 071102 (2018).
12. Q. Wang, X. Zhang, Y. Xu, Z. Tian, J. Gu, W. Yue, S. Zhang, J. Han, and W. Zhang, "A Broadband Metasurface-Based Terahertz Flat-Lens Array," Adv. Opt. Mater. **3**(6), 779–785 (2015).
13. X. Shen, Y. J. Wang, H. S. Chen, X. Xiao, Y. H. Lin, and B. Javidi, "Extended depth-of-focus 3D micro integral imaging display using a bifocal liquid crystal lens," Opt. Lett. **40**(4), 538–541 (2015).
14. H. S. Chen, Y. J. Wang, P. J. Chen, and Y. H. Lin, "Electrically adjustable location of a projected image in augmented reality via a liquid-crystal lens," Opt. Express **23**(22), 28154–28162 (2015).
15. W. Duan, P. Chen, S. J. Ge, B. Y. Wei, W. Hu, and Y. Q. Lu, "Helicity-dependent forked vortex lens based on photo-patterned liquid crystals," Opt. Express **25**(13), 14059–14064 (2017).
16. J. Beeckman, T. H. Yang, I. Nys, J. P. George, T. H. Lin, and K. Neyts, "Multi-electrode tunable liquid crystal lenses with one lithography step," Opt. Lett. **43**(2), 271–274 (2018).
17. C. S. Yang, T. T. Tang, P. H. Chen, R. P. Pan, P. Yu, and C. L. Pan, "Voltage-controlled liquid-crystal terahertz phase shifter with indium-tin-oxide nanowhiskers as transparent electrodes," Opt. Lett. **39**(8), 2511–2513 (2014).
18. L. Wang, X. W. Lin, W. Hu, G. H. Shao, P. Chen, L. J. Liang, B. B. Jin, P. H. Wu, H. Qian, Y. N. Lu, X. Liang, Z. G. Zheng, and Y. Q. Lu, "Broadband tunable liquid crystal terahertz waveplates driven with porous graphene electrodes," Light Sci. Appl. **4**(2), e253 (2015).
19. Y. Y. Ji, F. Fan, M. Chen, L. Yang, and S. J. Chang, "Terahertz artificial birefringence and tunable phase shifter based on dielectric metasurface with compound lattice," Opt. Express **25**(10), 11405–11413 (2017).
20. Z. Shen, S. Zhou, S. Ge, W. Duan, P. Chen, L. Wang, W. Hu, and Y. Lu, "Liquid-crystal-integrated metadevice: towards active multifunctional terahertz wave manipulations," Opt. Lett. **43**(19), 4695–4698 (2018).
21. Z. X. Shen, S. H. Zhou, S. J. Ge, W. Hu, and Y. Q. Lu, "Liquid crystal enabled dynamic cloaking of terahertz Fano resonators," Appl. Phys. Lett. **114**(4), 041106 (2019).
22. S. Ge, P. Chen, Z. Shen, W. Sun, X. Wang, W. Hu, Y. Zhang, and Y. Lu, "Terahertz vortex beam generator based on a photopatterned large birefringence liquid crystal," Opt. Express **25**(11), 12349–12356 (2017).
23. S. J. Ge, Z. X. Shen, P. Chen, X. Liang, X. K. Wang, W. Hu, Y. Zhang, and Y. Q. Lu, "Generating, Separating and Polarizing Terahertz Vortex Beams via Liquid Crystals with Gradient-Rotation Directors," Crystals (Basel) **7**(10), 314 (2017).
24. C. Y. Chen, C. L. Pan, C. F. Hsieh, Y. F. Lin, and R. P. Pan, "Liquid-crystal-based terahertz tunable Lyot filter," Appl. Phys. Lett. **88**(10), 101107 (2006).
25. L. Wang, S. Ge, W. Hu, M. Nakajima, and Y. Lu, "Graphene-assisted high-efficiency liquid crystal tunable terahertz metamaterial absorber," Opt. Express **25**(20), 23873–23879 (2017).
26. Y. Wu, X. Ruan, C. H. Chen, Y. J. Shin, Y. Lee, J. Niu, J. Liu, Y. Chen, K. L. Yang, X. Zhang, J. H. Ahn, and H. Yang, "Graphene/liquid crystal based terahertz phase shifters," Opt. Express **21**(18), 21395–21402 (2013).

Optics EXPRESS

27. P. Chen, L. L. Ma, W. Duan, J. Chen, S. J. Ge, Z. H. Zhu, M. J. Tang, R. Xu, W. Gao, T. Li, W. Hu, and Y. Q. Lu, "Digitalizing Self-Assembled Chiral Superstructures for Optical Vortex Processing," Adv. Mater. **30**(10), 1705865 (2018).
28. P. Chen, S. J. Ge, W. Duan, B. Y. Wei, G. X. Cui, W. Hu, and Y. Q. Lu, "Digitalized Geometric Phases for Parallel Optical Spin and Orbital Angular Momentum Encoding," ACS Photonics **4**(6), 1333–1338 (2017).
29. B. Y. Wei, W. Hu, Y. Ming, F. Xu, S. Rubin, J. G. Wang, V. Chigrinov, and Y. Q. Lu, "Generating switchable and reconfigurable optical vortices via photopatterning of liquid crystals," Adv. Mater. **26**(10), 1590–1595 (2014).
30. L. Wang, X. W. Lin, X. Liang, J. B. Wu, W. Hu, Z. G. Zheng, B. B. Jin, Y. Q. Qin, and Y. Q. Lu, "Large birefringence liquid crystal material in terahertz range," Opt. Mater. Express **2**(10), 1314–1319 (2012).
31. S. Wang, P. C. Wu, V. C. Su, Y. C. Lai, M. K. Chen, H. Y. Kuo, B. H. Chen, Y. H. Chen, T. T. Huang, J. H. Wang, R. M. Lin, C. H. Kuan, T. Li, Z. Wang, S. Zhu, and D. P. Tsai, "A broadband achromatic metalens in the visible," Nat. Nanotechnol. **13**(3), 227–232 (2018).
32. W. T. Chen, A. Y. Zhu, V. Sanjeev, M. Khorasaninejad, Z. Shi, E. Lee, and F. Capasso, "A broadband achromatic metalens for focusing and imaging in the visible," Nat. Nanotechnol. **13**(3), 220–226 (2018).
33. S. Wang, P. C. Wu, V. C. Su, Y. C. Lai, C. Hung Chu, J. W. Chen, S. H. Lu, J. Chen, B. Xu, C. H. Kuan, T. Li, S. Zhu, and D. P. Tsai, "Broadband achromatic optical metasurface devices," Nat. Commun. **8**(1), 187 (2017).
34. S. Wang, X. Wang, Q. Kan, S. Qu, and Y. Zhang, "Circular polarization analyzer with polarization tunable focusing of surface plasmon polaritons," Appl. Phys. Lett. **107**(24), 243504 (2015).
35. R. I. Stantchev, B. Sun, S. M. Hornett, P. A. Hobson, G. M. Gibson, M. J. Padgett, and E. Hendry, "Noninvasive, near-field terahertz imaging of hidden objects using a single-pixel detector," Sci. Adv. **2**(6), e1600190 (2016).
36. M. R. Andrews, P. P. Mitra, and R. deCarvalho, "Tripling the capacity of wireless communications using electromagnetic polarization," Nature **409**(6818), 316–318 (2001).
37. K. Kawase, Y. Ogawa, Y. Watanabe, and H. Inoue, "Non-destructive terahertz imaging of illicit drugs using spectral fingerprints," Opt. Express **11**(20), 2549–2554 (2003).
38. W. Xu, L. Xie, and Y. Ying, "Mechanisms and applications of terahertz metamaterial sensing: a review," Nanoscale **9**(37), 13864–13878 (2017).